Van der Waals epitaxial growth of few layers WSe2 on GaP(111) B

Niels Chapuis, Aymen Mahmoudi, Christophe Coinon, David Troadec, Dominique Vignaud, Gilles Patriarche, Pascal Roussel, Abdelkarim Ouerghi, Fabrice Oehler, Xavier Wallart

2D Materials

Van der Waals epitaxial growth of few layers WSe2 on GaP(111)B

To cite this article before publication: Niels Chapuis *et al* 2024 *2D Mater.* in press https://doi.org/10.1088/2053-1583/ad573a

Van der Waals epitaxial growth of few layers WSe_2 on $GaP(111)_B$

Niels Chapuis[1], Aymen Mahmoudi[2], Christophe Coinon[1], David Troadec[1], Dominique Vignaud[1], Gilles Patriarche[2], Pascal Roussel[3], Abdelkarim Ouerghi[2], Fabrice Oehler[2], Xavier Wallart[1*]

[1] Univ. Lille, CNRS, Centrale Lille, Junia, Univ. Polytechnique Hauts de France, UMR 8520-IEMN F59000 Lille France
[2] Université Paris-Saclay, CNRS, Centre de Nanosciences et de Nanotechnologies, 91120, Palaiseau, Paris, France
[3] Unité de Catalyse et de Chimie du Solide (UCCS), Université de Lille, CNRS, Centrale Lille, Université d'Artois, UMR 8181—UCCS, F-59000 Lille, France

Corresponding author: xavier.wallart@univ-lille.fr

Abstract

2D material epitaxy offers the promise of new 2D/2D and 2D/3D heterostructures with their own specific electronic and optical properties. In this work, we demonstrate the epitaxial growth of few layers WSe_2 on $GaP(111)_B$ by molecular beam epitaxy. Using a combination of experimental techniques, we emphasize the role of the growth temperature and of a subsequent annealing of the grown layers under a selenium flux on the polytype formed and on its structural and morphological properties. We show that a low growth temperature promotes the formation of the 1T' and 3R phases depending on the layer thickness whereas a higher growth temperature favours the stable 2H phase. The resulting layers exhibit clear epitaxial relationships with the $GaP(111)_B$ substrate with an optimum grain disorientation and mean size of 1.1° and around 30 nm respectively for the 2H phase. Bilayer 2H $WSe_2/GaP(111)_B$ heterostructures exhibit a staggered type II band alignment and p-doped character of the epi-layer on both p and n-type GaP substrates. This first realisation of stable p-type WSe_2 epi-layer on a large-area $GaP(111)_B$ substrate paves the way to new 2D/3D heterostructures with great interests in nanoelectronic and optoelectronic applications, especially in the development of new 2D-material p-n junctions.

Keywords: 2D materials, Molecular Beam Epitaxy, Van der Waals epitaxy, 2D on 3D heterostructure, WSe_2, X-ray Photoelectron Spectroscopy

1. Introduction

For two decades and beyond graphene [1], 2D materials interests have tremendously increased and especially Transition Metal Dichalcogenides (TMDCs) because of their remarkable electrical and optical properties [2–4]. Semiconducting ones such as MoS_2, $MoSe_2$, WS_2 or WSe_2 show an indirect to direct band gap transition when the film thickness is reduced from multilayer to monolayer[5–7], making them very promising for the development of new generation electronic and opto-electronic devices [2,3,8,9]. WSe_2 appears particularly interesting due to large spin-orbit coupling and spin-splitting in the K valley [10,11] as well as a high carrier mobility [12,13].

Those physical properties have been widely studied on mechanically or chemically exfoliated micron-sized TMDCs flakes. On the other hand, well-developed bottom-up approaches like Chemical Vapor Deposition (CVD) demonstrated high crystalline quality TMDC monolayer [14–17] with high carrier mobility for flakes up to hundreds micrometres wide. Yet, large area monocrystalline TMDC growth remains a clear issue. Among some alternative methods, Molecular Beam Epitaxy (MBE) has demonstrated valuable results for the growth of WSe_2 and related heterostructures, especially on 2D-substrates, because of the natural van der Waals interface between the epi-layer and the substrate surface. Therefore, a large amount of studies have focused on WSe_2 epitaxy on HOPG [18–20] or graphene bilayer [21,22], underscoring specific electrical and structural properties. Notably, it has been shown that a low growth temperature (~230°C) would favour the formation of metastable 1T'-WSe_2 phase which exhibits a quantum spin Hall Effect as well as a metallic behaviour [23]. On the other hand, a significantly higher temperature (~400°C) is required to promote the stable and semiconducting 2H-WSe_2 phase [23]. A third stable stacking order with ferroelectric properties is the 3R-WSe_2 phase [24,25]. Recently Vergnaud *et al.* have investigated WSe_2 growth on mica, pointing out the importance of the use of very low deposition rate and high temperature (around 900°C) to improve the average grain size and crystalline orientation [26], as suggested by the Monte-Carlo simulation study performed by Nie et *al.* [27]. On the other hand, new generation of heterojunction have emerged, using 3D substrates such as insulating sapphire $Al_2O_3(0001)$ [28,29] or AlN(0001) [30], underlining the importance of surface preparation prior growth. Lately, Pierucci *et al.* [31] have demonstrated scalable monolayer thick and highly oriented WSe_2 film on top of $GaAs(111)_B$, showing evidence of a high p-type doping due to charge transfer from the GaAs substrate. On the same substrate, Ohtake *et al.* [32] have successfully grown large-area and highly oriented $MoSe_2/WSe_2$ heterostructures, creating new interests in

the use of III-V semiconductors as substrates for TMDC growth, especially for opto-electronic devices development. Both studies also highlight the need for a termination of the surface dangling bonds with selenium prior to WSe_2 growth in order to favour the formation of a Van der Waals gap [33–36]. This process has been widely discussed since the 1990's for growing semiconducting chalcogenides such as GaSe [37,38] or $MoSe_2$ [33] on top of GaAs.

In this work, we investigate the growth of WSe_2 films on $GaP(111)_B$ substrates, as GaP shows a similar crystallographic structure as GaAs but exhibits a significantly higher thermal stability [39] with a congruent sublimation temperature at 675°C [40] instead of 625°C [41]. This structural feature should allow us reaching higher growth temperatures, and therefore result in increasing the nucleus size, leading to larger grains and higher carrier mobility [27]. Thus, we focus this study on the impact of the growth and annealing temperatures on the crystal structure quality, the surface morphology and the different WSe_2 polytypes formation.

We report the epitaxy of continuous, large-area, semiconducting few layers WSe_2 on Se-terminated $GaP(111)_B$. We point out the formation of the metastable 1T' and 3R phases at low growth temperature (T_G) and the formation of metallic W-W bonds at T_G exceeding 500°C. We underscore the importance of T_G and the need for applying a subsequent annealing step under a Se flux in order to promote the semiconducting 2H phase formation. An optimal WSe_2 2H bilayer grown between 450°C and 500°C, annealed at 650°C, exhibits a flawless interface, a 1.1° in-plane disorientation and a mean grain size of ~30 nm. We highlight the systematic p-type doping of the epi-layer, and a staggered band alignment with a slight variation of the band offset depending on the initial substrate doping type.

2. Experimental

For this study we use 1/6 of 2 inch $GaP(111)_B$ substrates from Ensemble3 Ltd. Poland cleaved and then glued with indium on 3-inch unpolished Si wafer. The substrate is first outgassed for 90 minutes at 200°C under ultra-high vacuum (UHV) and then transferred to a III-V dedicated MBE chamber for deoxidization at 550°C using both atomic hydrogen and cracked phosphine. This results in a clear and sharp 2×2 Reflection High Energy Electron Diffraction (RHEED) pattern. The sample is then transferred under UHV to a second MBE reactor dedicated to TMDC growth fitted with a Riber VCOR 110 valve cracker cell for selenium sublimation and a Telemark electron gun as tungsten source.

Before WSe_2 growth, the selenium beam equivalent pressure and tungsten growth rate are respectively measured thanks to a Bayard-Alpert flux gauge and a quartz microbalance, placed close to the sample position and the deoxidized GaP substrate surface is passivated under a selenium flux at a minimal temperature of 450°C. The RHEED pattern evolves from a 2×2 to a 1×1 one a few seconds after selenium introduction. According to Atomic Force Microscopy (AFM) measurements, the resulted RMS roughness is around 0.2 nm. Throughout this study, the tungsten growth rate is fixed at 0.002 Å/s ± 15%, the Se flux is set at $2\text{-}5\times10^{-6}$ Torr for the growth process, and the temperature varies between 250°C and 650°C. The WSe_2 surface crystallography is monitored during growth by *in situ* RHEED, whereas complementary analysis is performed using Low Energy Electron Diffraction (LEED) at 50 eV.

For X-Ray and ultra-violet photoelectron spectroscopy (XPS, UPS) analysis, the sample is transferred under UHV after growth in a surface analysis chamber equipped with a Physical electronics 5600 system. XPS measurements are performed with a monochromatic Al Kα (1486.6 eV) X-Ray source for which the ultimate overall resolution as measured from the full width at half maximum (FWHM) of the Ag $3d_{5/2}$ line is 0.5 eV. The acceptance angle of the hemispherical analyser is set to 14° and the angle between the incident X-Rays and the analyser is 90°. The direction of photoelectrons is given by the polar angle θ, as referenced to the sample surface and the azimuth angle φ. To obtain depth dependent measurements, three polar angles, i.e. 25, 45, 75° are chosen whereas the azimuth angle is fixed along the sample <112> direction. Estimation of the grown WSe_2 film thickness was based on the ratio between the W 4f and Ga 3d XPS core levels (CL) line intensities for the three polar angles and the related electron attenuation lengths [42–46]. The intensity of the various XPS are measured as the peak area after standard background subtraction according to the Shirley procedure [47,48]. Core level decomposition is achieved using pseudo-Voigt functions within the PHI MultiPak™ software [49]. The branching ratios are theoretical ones and the splitting energies are fixed at 0.86 eV between Se $3d_{5/2}$ and Se $3d_{3/2}$, and 2.16 eV between W $4f_{7/2}$ and W $4f_{5/2}$. A He I Kα (21.2 eV) source is used for UPS analysis and valence band spectra are recorded around the Γ point of the Brillouin zone. The valence band maximum (VBM) is determined through the intercept of a linear extrapolation of the decreasing density of states with the baseline. For work function determination, the sample is biased at -3 V and the threshold energy is measured as the intercept of a linear interpolation of the rapidly rising intensity with the baseline.

The surface morphology is investigated by *ex situ* Atomic force Microscopy (AFM) on a Multimode model from Bruker monitored with a Bruker NS4a controller in tapping mode using standard NCHVA-A probes from Bruker with a resonance frequency at ~320 kHz.

For Scanning Transmission Electron Microscopy (STEM), Raman and X-Ray Diffraction (XRD) studies, the samples are capped with an amorphous selenium layer. After preparation of thin slabs using focus ion beam (FIB) etching, STEM studies are performed in a Titan Themis 200 (FEI) microscope equipped with a spherical aberration corrector on the probe and an energy-dispersive x-ray spectroscopy (EDX) system super X (0.7 srad solid angle of collection). The accelerating voltage is 200 kV. The (half) convergence angle of the probe is 17.6 mrad and the probe current 40-45 pA. The inner and outer semi-angles of the Dark Field detector are respectively 69 mrad and 200 mrad, detecting inelastically scattered electrons at high angles (HAADF-STEM images).

Raman spectroscopy analysis is performed on a Horiba Scientific LabRAM HR instrument with a laser wavelength of 473.1 nm. The spectral resolution is 0.5 cm^{-1} for a grating with 1800 grooves per mm. The FWHM of the different Raman components are extracted through the best fit of the experimental spectra, after subtracting the substrate contribution, with Lorentzian functions.

Finally X-Ray diffraction (XRD) measurements in grazing incidence are achieved using a SmartLab Rigaku diffractometer to quantify the in-plane disorientation and estimate the mean grain size after growth by recording 2 spectrum types : azimuthal φ scans and $2\theta_{\chi/\varphi}$ scans. The X-ray beam is generated from a copper rotating anode (Cu $K\alpha_{1,2}$ = 1.5418 eV) and equipped with in-plane collimators, leading to an angular resolution of 0.114°.

3. Results and discussions

3.1. Impact of the growth temperature and the film thickness

We investigate the impact of the growth temperature on the nucleation step by comparing the evolution of the surface morphology at 250°C and 450°C for the same nominal deposited thickness around 0.25 ML (**Figure S1a & S1b**), which shows that raising T_G from 250°C to 450°C reduces the WSe_2 nuclei density. This trend underscores the increase of the species surface diffusion with T_G. It also reveals that the nucleation does not occur at particular preferential sites such as atomic step edges but rather all over the surface. Together with the

small grain size reached at 450°C, this shows that surface diffusion remains limited in the explored T_G range as expected for tungsten-based species.

Monolayer WSe_2 exhibits the most stable trigonal prismatic 1H phase or the metastable orthorhombic 1T' one, arising from a distortion of the octahedral 1T phase [23]. The most stable stacking for multilayer are the 2H and 3R ones. Within the 2H stacking (AA' configuration), the W(Se) atoms of one layer reside above or below the Se(W) atoms of another layer. Within the 3R stacking (AB configuration), this superposition occurs only for half of the W and Se atoms. These different phases and stacking orders can be identified through STEM observations performed along the GaP [1-10] zone axis. Indeed, the Se-W-Se bonds in the 1H phase are characterized by herringbones whereas they exhibit distorted parallel segments in the 1T' one. For multilayer, the 2H stacking order results in alternated herringbones directions from one layer to another, while the herringbones will keep their orientation for the 3R stacking, exhibiting only a translation between different layers.

FIGURE 1a shows the RHEED pattern after a bilayer growth at T_G=250°C along the two main directions, which clearly follows a two dimensional mode with the unique presence of vertical streaks, resulting in a smooth surface (RMS~0.3 nm) and small domains observed in AFM (**FIGURE 1b**). Thus in this case, the presence of intermediate lines on the RHEED pattern, close to a 2×2 reconstruction indicates the presence of the metastable 1T' phase [23]. Intermediate dots on the LEED patterns for both monolayer and bilayer WSe_2 (**FIGURES 1c & 1d**) confirm the presence of this 1T' phase. HR-STEM images in the high angle annular dark field (HAADF) mode along the (110) zone axis for a sub-monolayer sample in **FIGURE 1e** bring additional proof of this 1T' phase coexisting with a disordered 1H one. This latter exhibits a high in-plane disorientation as two different 1H orientations are resolved within the same image. For the bilayer, HR-STEM observation mainly points out the formation of a rhombohedral stacking (**FIGURE 1f**). Along the same line, based on TEM observations supported by ARPES and micro-Raman measurements [50], Mahmoudi et *al.* have shown that a WSe_2 bilayer epitaxially grown on n-type $GaP(111)_B$ at 250°C exhibits a preferential 3R-bilayer stacking with still a small amount of 1T' in the top layer. For this bilayer, we decompose the W 4f and XPS CL with a first doublet at 32.44 eV linked to the 3R phase [51] and a second doublet for 1T' with a binding energy shift of -0.60 eV [22,52] (**FIGURE 1g**). It highlights the coexistence of a dominant 3R phase and a residual 1T' one (<10%) in a 250°C grown WSe_2 bilayer. In comparison, the W 4f CL for a 0.6 ML sample shows a clear dominance of the 1T' phase over the 1H one (**Figure S2a**). The Se 3d CL (**FIGURE 1h**) also exhibits two doublets

with the main one at 54.61 eV. In this case, the origin of the second low binding energy doublet can be ascribed to both the 1T' phase and to selenium atoms bonded to gallium ones at the top surface of the selenium passivated GaP substrate.

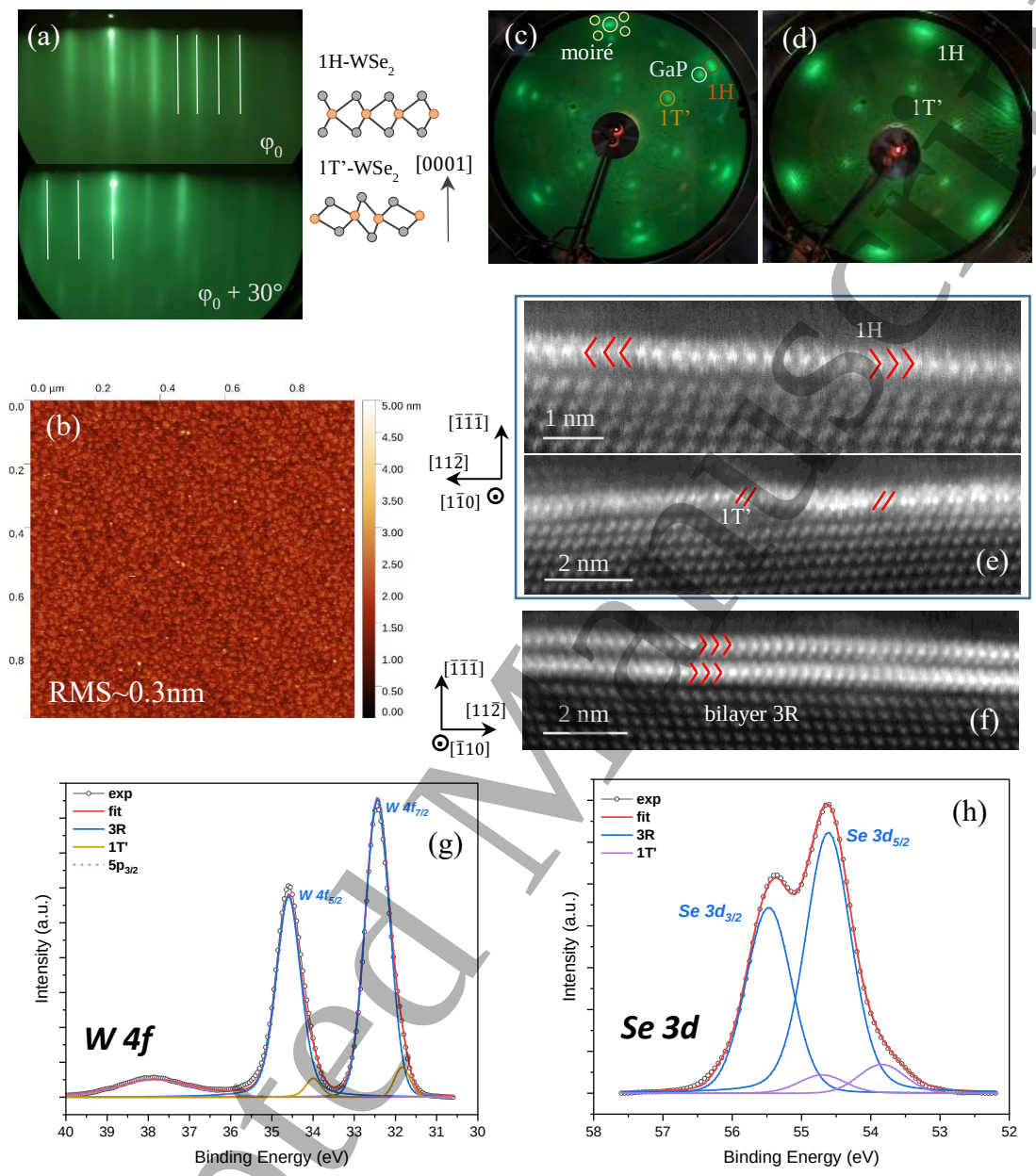

Figure 1: surface and interface characterization of a WSe_2 monolayer and bilayer grown at T_G=250°C: *(a) RHEED pattern along the two primary directions rotated by 30° of 2ML WSe_2 grown at T_G=250°C on an n-type GaP substrate and (b) corresponding AFM image; 50 eV LEED pattern evolution at 1ML (c) and 2MLs (d). HAADF STEM image of 1ML (e) and 2MLs (f); 1T' and 1H stacking side view schematic adapted from [23]. Red herringbones and lines are representing 1H and 1T' phases, respectively. Decomposition of W 4f (g) and Se 3d (h) CL recorded at θ=25° for a 2ML growth.*

This latter exhibits a clear van der Waals gap with the epi-layer as revealed by a close look at the interface (**FIGURE 1f**). As the brightness contrast in HAADF is roughly proportional to the square of the atomic number (~Z^2), the contrast observed at the interface reveals an extreme GaP surface selenium passivation before growth and validates the surface treatment used to get a $GaP(111)_B$-Se pseudo van der Waals substrate. Overall, at this temperature, TEM images show a good substrate to epi-layer interface with no apparent issues during the early selenium passivation, also confirmed by the presence of a moiré for the monolayer growth in LEED, whose continuity is not disturbed by atomic edges (**FIGURE 1e**).

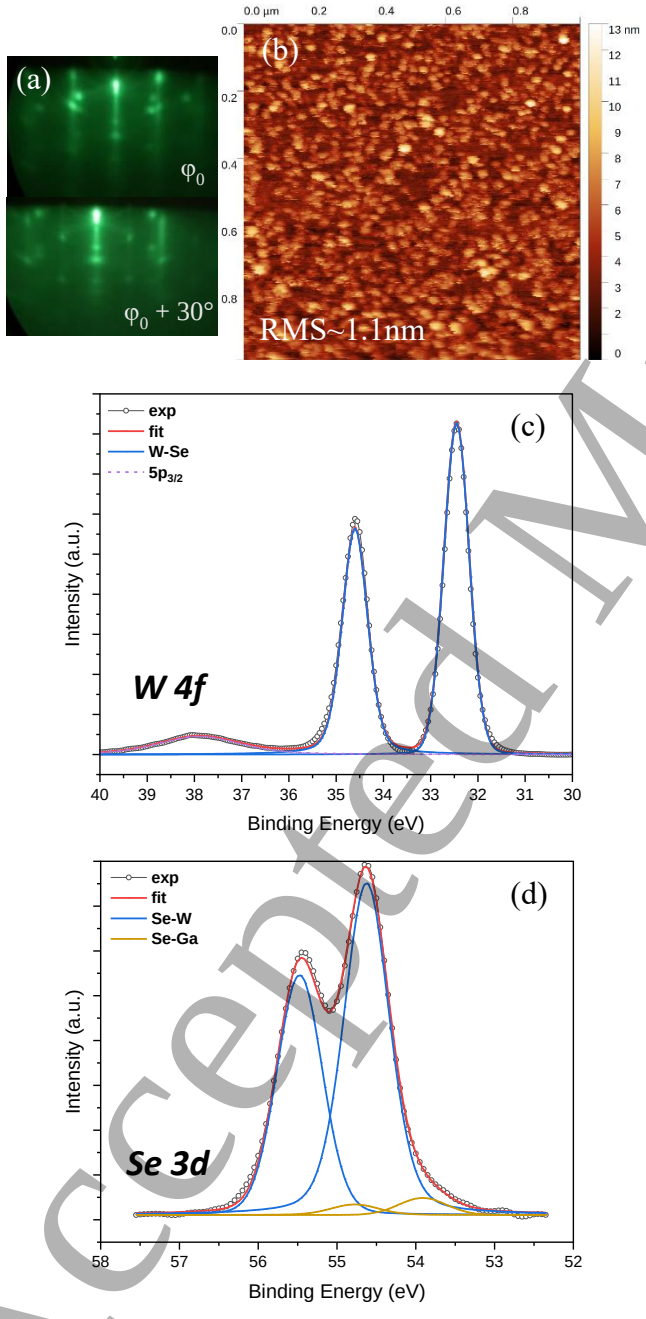

Figure 2: Surface characterization of a WSe_2 bilayer grown at T_G=450°C: *(a) RHEED pattern along the primary directions of a 2 ML WSe_2 grown on an n-type GaP substrate and associated AFM image (b); W 4f CL (c) and Se 3d CL (d) decompositions. XPS CLs are measured at a takeoff angle θ=25°.*

Contrarily, increasing T_G up to 450°C favours a three dimensional growth mode with the presence of additional spots along and around the 1×1 RHEED WSe_2 streaks (**FIGURE 2a**), resulting in a quite rough surface (RMS~1.1 nm) with 25 nm wide domains (**FIGURE 2b**). Actually, the 3D behaviour appears at the end of the first monolayer growth with a slow degradation of the RHEED pattern. A similar behaviour is observed at T_G=500°C. The suppression of the 1T' phase suggested by the disappearance of the intermediate lines in RHEED is further confirmed by W 4f and Se 3d CLs deconvolution (**FIGURE 2c & 2d**) which exhibits a single component at 32.41 eV and 54.62 eV related to the stable WSe_2 [30,53] phase.

The second doublet at 53.8 eV in the Se 3d spectrum is linked to surface Ga-Se bonds induced by the early selenium passivation of the GaP substrate [31,53].Increasing T_G up to 550°C reduces even more the 1×1 reconstruction with a quasi-fully 3D growth mode. Moreover, the W 4f XPS CL decomposition at T_G=550°C (**Figure S2b**) exhibits a second component at lower binding energy (BE) around 31.8 eV, correlated to metallic tungsten [54,55], indicating a lack of selenium above 500°C, favouring the formation of metallic W clusters. Considering the strong Se overpressure used, this is probably due to excessive selenium re-evaporation from the surface at this temperature. These observations lead us to reduce the upper limit of T_G down to 500°C.

3.2. Impact of annealing under selenium flux at 650°C

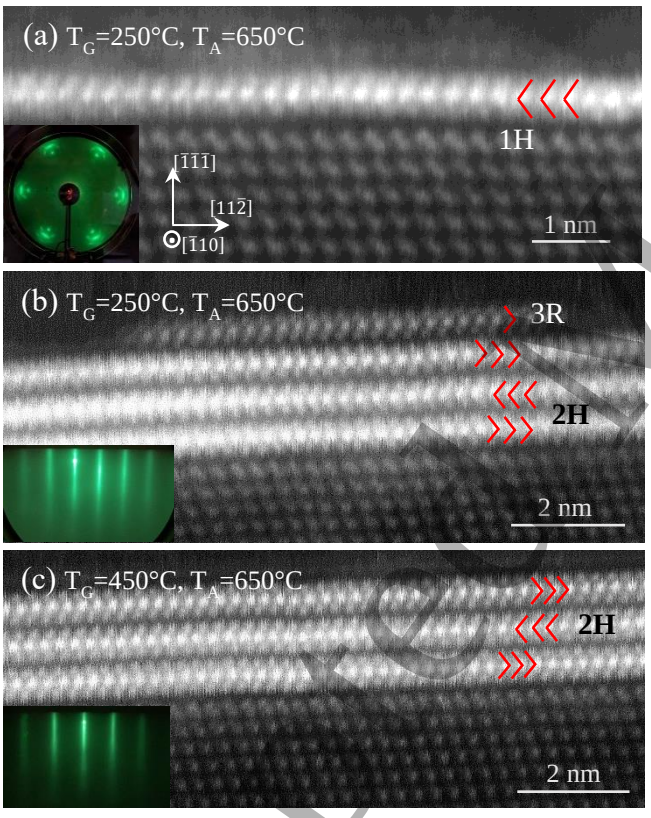

Figure 3: Impact of Se-annealing treatment at T_A=650°C: *HAADF STEM images for 1ML (a) 3MLs (b) grown at T_G=250°C and for 3MLs grown at T_G=450°C (c). Insets show the corresponding LEED (a) and RHEED (b, c) patterns.*

As presented above, direct growth of WSe_2 on top of GaP(111)$_B$-Se exhibits specific features depending on the temperature. In the following section, we are investigating the impact of an annealing under selenium flux on the phases formed as well as on the film morphology and structure. The temperature ramp after the growth is set at 20°C/min and the sample is maintained at T_A=650°C for 5-10 minutes before decreasing the temperature. We close the selenium shutter only once the substrate temperature has decreased below 450°C, in order to limit any desorption or accumulation of Se on the surface. For all the results presented below, the main evolution of the RHEED pattern occurs once the substrate temperature reaches a minimum of 630°C.

The annealing of a 1 ML and 3 ML thick WSe_2 films grown at 250°C leads to the total suppression of the metastable 1T' phase, as

evidenced by the observed 1x1 RHEED and LEED pattern (**FIGURE 3a & 3b**). This is further confirmed by the STEM observation, which clearly demonstrates the formation of the 1H phase in the case of a monolayer growth. We further notice that the annealing does not alter the van der Waals interface. In the case of a 3 ML growth, the 2H and the 3R-bilayer stacking are observed within the same TEM image, with a 3R-bilayer formation on the top surface partial layer. AFM imaging after 650°C annealing of a WSe_2 bilayer grown at 250°C (**Figure S3a**) shows a slight decrease of the roughness (0.2 vs 0.3 nm) and the appearance of GaP atomic steps in the background, indicating a good epitaxial relation. In addition, XPS W 4f and Se 3d (**FIGURE 4a & 4b**) CLs spectra measured before and after annealing the sample confirm the suppression of the 1T' phase. Besides, Raman shift measurements (**FIGURE 4c**) highlights a 3R/2H mix phase by the observation of two distinct vibrations modes: a main A_{1g} at 251.2 cm^{-1} (FWHM=3.1 cm^{-1}) and a secondary degenerated E^1_{2g} at 247.9 cm^{-1} (FWHM=4.5 cm^{-1}) [51,56,57] with a E^1_{2g}/A_{1g} area ratio equal to 0.87. The additional peak observed at 239 cm^{-1} is linked to the crystallized Selenium cap.

On the other hand, the morphology of annealed 3 ML thick WSe_2 layers grown at 450°C is greatly improved, as suggested by the 1 × 1 streaky 2D RHEED pattern (**FIGURE 3c**) and the AFM images (**Figure S3b**), showing a reduction of the roughness. In these cases, STEM observations (**FIGURE 3c**) demonstrate the formation of a bi-dimensional 2H phase layer. Combining the RHEED and STEM observations, the epitaxial relationships are [11-20]WSe_2//[1-10]GaP, [1-100]WSe_2//[11-2]GaP in-plane and [0001]WSe_2//[-1-1-1]GaP out of plane. The comparison of the W 4f and Se 3d CLs signals before and after annealing (**FIGURE 4a & 4b**) confirms a reduction of the peak width at 450°C (from 630 meV to 540 meV, and from 680 meV to 570 meV, respectively), which we can link to crystal quality improvement. Only one single doublet at 32.4 eV [30,53] is required for the W 4f CL fitting (**FIGURE 4d**). The Se 3d CL decomposition (**FIGURE 4e**) shows three doublet, a first one at 54.55 eV linked to 2H-WSe_2 and a second at 53.85 eV linked to surface GaSe induced by the early selenium passivation. The third doublet at 55.15 eV is attributed to some excess Se accumulated at the surface during the cooling down following the annealing process. Raman shift measurement in **FIGURE 4c** shows a slight reduction of the E^1_{2g} peak intensity (E^1_{2g}/A_{1g}=0.65) at T_G=450°C compared to T_G=250°C (E^1_{2g}/A_{1g}=0.87). Therefore, a combination of high growth temperature and annealing at 650°C under selenium flux tend to favour the formation of single 2H phase for a few layers WSe_2 film. A closer look at the interface reveals no peculiar degradation due to the annealing step for T_G=250°C and 450°C.

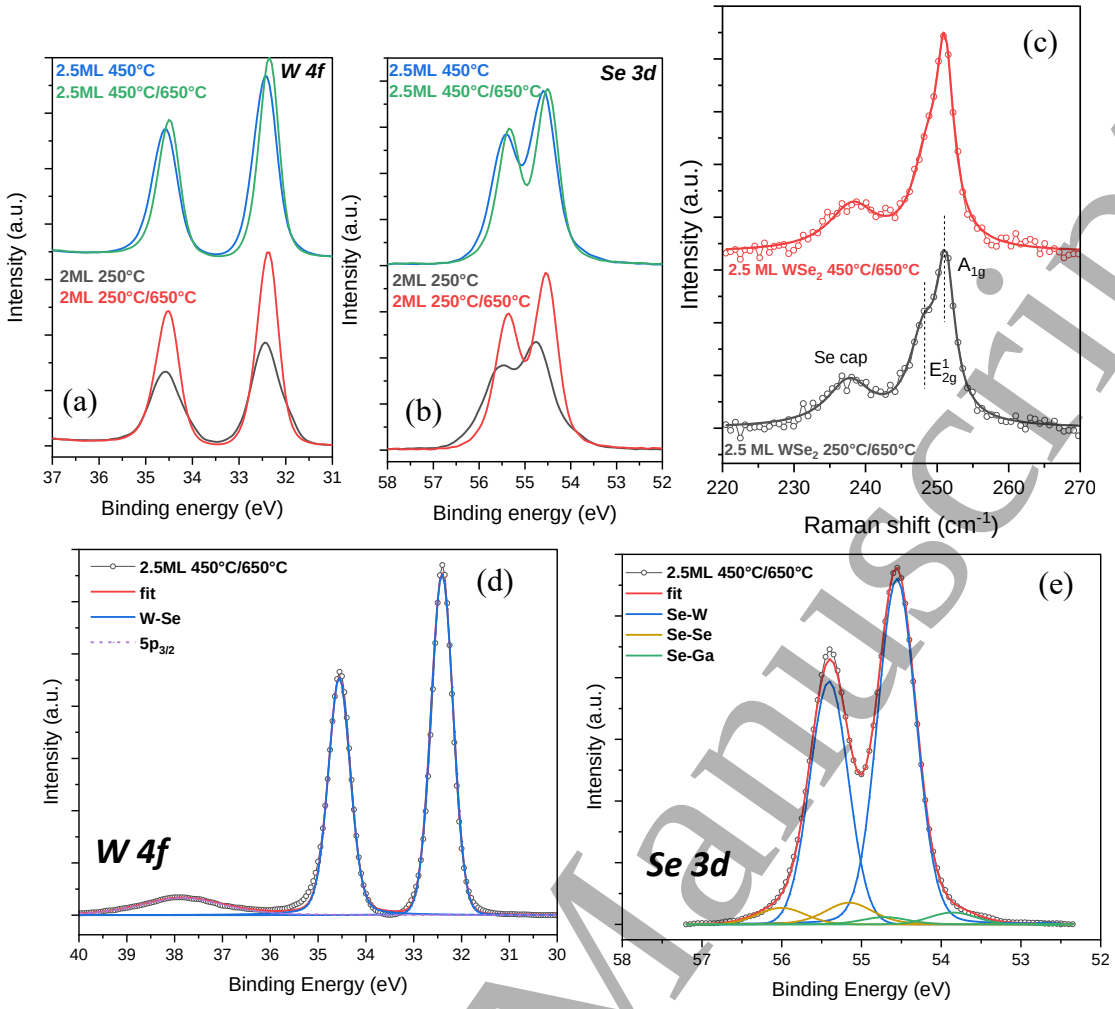

Figure 4: Impact of Se-annealing treatment at T_A=650°C: *W 4f CL (a), Se 3d (b) and Raman shift (c) evolutions. Decomposition of W 4f CL (d) and Se 3d CL (e) spectra recorded with a take-off angle θ=25° on an n-type GaP substrate.*

Grazing incidence in-plane XRD global φ and $2\theta_{\chi/\varphi}$ scans (**FIGURE 5a & 5b**) highlight the alignment of WSe_2 grains with the GaP symmetry axes. Then, we estimate the average grain size of WSe_2 from plotting the FWHM of (1 0 0), (2 0 0) and (3 0 0) peaks at $2\theta_{\chi/\varphi}$ = [31.4°; 65.3°; 108.1°], respectively [26,31], using the Williamson-Hall technique [58] as presented in the **Figure S4a**. On the other hand, the in-plane angular spread is measured as the FWHM of the most intense [1-10] ($2\theta_{\chi/\varphi}$=55.9°) φ_{WSe2} peak for each sample. The evolution of both parameters with T_G, the Se-annealing treatment and the tungsten growth rate is summarized in **TABLE 1**. An annealed WSe_2 bilayer grown at 250°C shows a rather high in-plane disorientation of 2.53° and a small average grain size around 15 nm. In **FIGURE 5c and 5d**, we plot the most intense [1-10] φ_{WSe2} and the XRD (100) $2\theta_{\chi/\varphi}$ peaks (31.4°), respectively, for

different growth conditions. It appears clearly that increasing T_G up to 450°C enlarges the

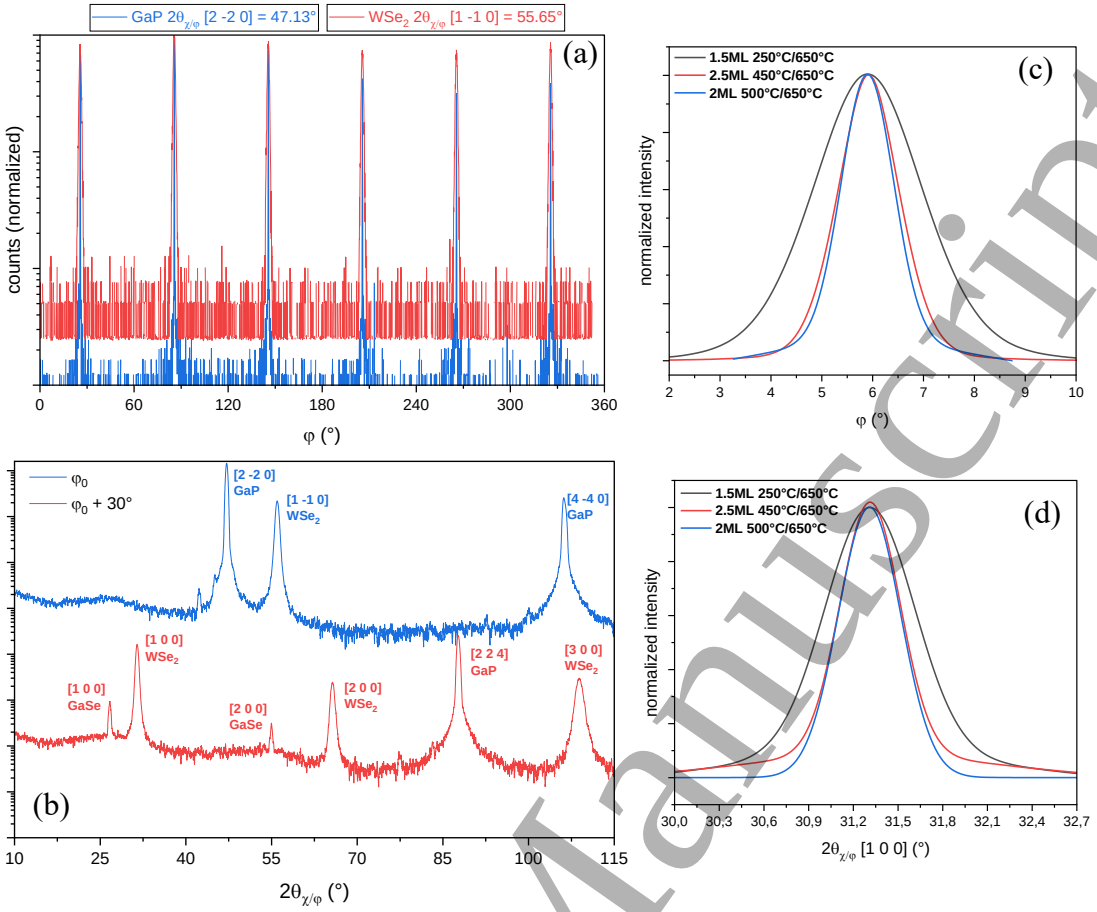

Figure 5: influence of T_G and Se-annealing treatment on grain size and in-plane disorientation measured with grazing incidence XRD: *(a) 360° GaP ($2\theta_{\chi/\varphi}$=47.13°) and WSe_2 ($2\theta_{\chi/\varphi}$=55.69°) azimuthal φ pattern for a WSe_2 bilayer grown at T_G=450°C and Se-annealed (b) XRD $2\theta_{\chi/\varphi}$ diffractogram along two azimuthal directions. Evolution of normalized (c) WSe_2 φ and (d) $2\theta_{\chi/\varphi(100)}$ scans with T_G after annealing.*

average grain size up to 23 nm, correlated to a reduction of the $2\theta_{\chi/\varphi}$ FWHMs$_{(100)}$. In an attempt to get larger grains, we further rise T_G up to 500°C but it does not show any clear improvement with respect to 450°C resulting in a somewhat comparable grain of 23 nm. Contrarily, the in-plane disorientation seems to be more sensitive to T_G, as it decreases from 1.75° for T_G=450°C to 1.48° for T_G=500°C. Furthermore, applying a Se-annealing treatment after a growth at 450°C or 500°C exhibits a similar behaviour, with a rather stable average grain size of ~23 nm and a decreased of the disorientation to 1.43° and 1.25°, respectively. Therefore, we will assume that at a defined T_G, the Se-annealing treatment mainly enhance the in-plane disorientation, whereas the mean grain size is rather defined by T_G with an optimum for a growth between 450°C and 500°C. On the other hand, increasing the growth rate up to ~0.02 Å/s degrades both the grain disorientation and mean size regardless of T_G. Indeed, increasing the growth rate will tend to

increase the nuclei density and reduce their size, which is why we use a low tungsten growth rate (~0.002 Å/s) throughout this work.

Last, the 3D behaviour observed by RHEED during growth at 450°C or 500°C can be largely reduced by interrupting the growth and annealing under Se at 650°C after the first monolayer. RHEED observations during the second monolayer suggest a 2D growth with little presence of additional spots along the 1 × 1 streaks. A second annealing step is performed after the bilayer growth, resulting in the reduction of the final disorientation down to 1.07°. In this case, we estimate an optimal average grain size of 32 nm for a WSe_2 bilayer grown at 500°C with a 2-step annealing (**TABLE 1**). Overall, the WSe_2 layers grown at 450°C or 500°C with a low growth rate and subsequent Se-annealing step at 650°C exhibits the best features with very close XPS spectra and average grain size. In addition, Raman spectroscopy measurements over a centimetre-scaled surface evidence the good uniformity of the WSe_2 growth, as presented in **Figure S5**.

sample	Grain size (nm)	In-plane disorientation Δφ (°)
2.5 ML 250°C/650°C 0.02 Å/s	15±4	2.93±0.02
1.5 ML 250°C/650°C 0.002 Å/s	15±1	2.53±0.03
2 ML 450°C 0.002 Å/s	22±7	1,75±0,02
2.5 ML 450°C/650°C 0.02 Å/s	17±4	2.17±0.01
2.5 ML 450°C/650°C 0.002 Å/s	25±10	1.43±0.01
2 ML 500°C 0.002 Å/s	23±9	1.48±0.03
2 ML 500°C/650°C 0.002 Å/s	23±1	1.25±0.01
2x1 ML 500°C/650°C 0.002 Å/s	32±10	1.07±0.01

Table 1**: **Average grain size and in-plane disorientation evolution with T_G, T_A and the growth rate based on XRD measurements**. A comparison of WSe_2 $2\theta_{\chi/\varphi(100)}$ and φ signals is presented in **Figures S4b to S4d.

3.3. Band structure

In this section, we discuss the band structure of a WSe_2 bilayer grown on a $GaP(111)_B$ at 450°C and start with the results relative to a p-type ($p \sim 6\text{-}7\times10^{17}$ cm^{-3}) substrate. We calculate the valence band discontinuity (ΔE_V), measure the work function (Φ) and the energy of the valence band maximum (VBM), and finally draw the band alignment assuming a GaP bandgap and an electron affinity of 2.26 eV and 3.8 eV respectively[59].

The valence band discontinuity ΔE_V is extracted using the Waldrop method [60,61] which stands from the following equation: $\Delta E_V = \Delta E_{CL} + \left(E_{P2p}^{GaP} - E_V^{GaP}\right) - \left(E_{W4f}^{WSe_2/Cg} - E_V^{WSe_2/Cg}\right)$. On a deoxidized GaP(111)$_B$ substrate, we measure the binding energy of the P 2p CL E_{P2p}^{GaP} and the energy of the top of the valence band E_V^{GaP} by XPS at θ=75° in such a way that $\left(E_{P2p}^{GaP} - E_V^{GaP}\right) = 128.00 \pm 0.05\ eV$. In the same way, we get $\left(E_{W4f}^{WSe_2/GaP} - E_V^{WSe_2/GaP}\right) = 31.71 \pm 0.05\ eV$ recorded on a bulk WSe_2 (~15 ML) grown at 450°C and Se-annealed on a GaP(111)$_B$-Se substrate. On the other hand, the ΔE_{CL} value is extracted by measuring the binding energy difference between W $4f_{7/2}$ and P $2p_{3/2}$ CLs on the p-GaP/WSe_2 heterostructure, which results in $\Delta E_{CL_{p-GaP/WSe_2}} = -97.02 \pm 0.05\ eV$ and induces a $\Delta E_{V_{p-GaP/WSe_2}}$ of $-0.73 \pm 0.1\ eV$. Measurement of these three values are presented in **Figure S6a to S6c**.

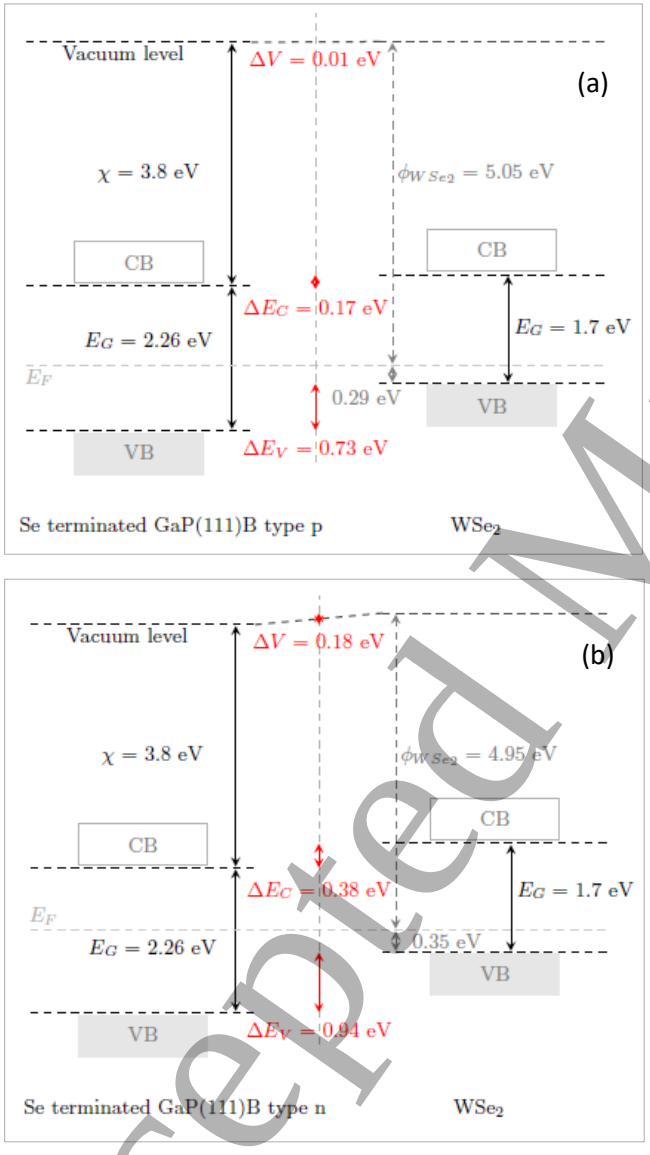

Figure 6: Band structure schematic: *(a) 2 MLs WSe_2/p-GaP(111)$_B$ heterojunction. (b) 2 MLs WSe_2/n-GaP(111)$_B$ heterojunction.*

For this heterostructure, UPS measurements around the Γ point indicates the energy of the VBM at $0.29 \pm 0.05\ eV$. Thus, assuming an electronic bandgap between 1.7 eV [50] and 1.8 eV [18] for a WSe_2 bilayer, it expresses a p-type doping of the epi-layer. On the other hand, the work function determined from the threshold energy measurement as: $E_{th} = h\nu + eV_p - \Phi$ where V_p is the bias voltage of the substrate (-3 V), leads to $\Phi = 5.05 \pm 0.05\ eV$. UPS measurements are presented in **Figure S7a**. Therefore, the final arrangement of the heterojunction represented in **FIGURE 6a** exhibits a staggered gap

between WSe_2 and GaP, qualified as a type-II band alignment with nearly no charge transfer at the interface.

In comparison, the band structure of a GaP/WSe_2 heterostructure on a n-type GaP(111)$_B$ substrate (n~2-3×10^{18} cm^{-3}) is also determined. In this case, the extracted band offset is larger than previously, with $\Delta E_{CL_{n-GaP/WSe_2}} = -97.23 \pm 0.05\ eV$, leading to $\Delta E_{V_{n-GaP/WSe_2}} = -0.94 \pm 0.1\ eV$. This difference between n-type and p-type GaP(111)$_B$/WSe_2 heterojunction is supposed to come from the van der Waals nature of the substrate/epi-layer interface. Indeed, a difference in the surface dipole between n and p-type GaP(111)$_B$ surfaces after the Se-passivation treatment prior growth could explain the band offset difference. This observation is in good agreement with previous ones, showing that the band offset of GaAs/MoS_2 [62] and GaAs/WSe_2 [31] heterojunctions changes depending on the doping type of GaAs. UPS measurements in **Figure S7b** expresses a p-type doping of the epi-layer with $E_{WSe_2/n-GaP} - E_F = 0.35 \pm 0.05\ eV$ and a work function $\Phi = 4.95 \pm 0.05\ eV$. Thus, the final arrangement of the heterojunction exhibits also a type-II band alignment more staggered than previously with a slight electron charge transfer at the interface of potential step ΔV=0.18 eV (**FIGURE 6b**). This peculiar type-II band alignment might be suitable for the development of future tunnelling or photodetector devices[63,64].

4. Conclusion

In summary, we have demonstrated the growth of few layers WSe_2 on top of Se-terminated GaP(111)$_B$ using MBE, resulting in a quasi van der Waals 2D/3D heterojunction. The WSe_2 epi-layer exhibits a total surface coverage with continuity over atomic step edges. We have underscored the importance of the growth temperature and of a post-growth annealing step under Se flux on the phase formation, surface morphology, grain in-plane disorientation and mean size, with the best semiconducting WSe_2 bilayer grown between 450°C and 500°C, and annealed at 650°C. This results in the formation of single phase 2H-WSe_2 with a flawless interface, a 1.1° in-plane disorientation and a mean grain size of ~30 nm. Furthermore, XPS and UPS measurements demonstrate an intrinsic p-type doping of the epi-layer and a staggered type-II band alignment at the WSe_2/GaP(111)$_B$ interface, regardless of the initial substrate doping type. On the other hand, we have observed a 0.2 eV band offset difference between n-type GaP and p-type GaP heterojunctions. This first realisation of stable p-type WSe_2 epi-layer

on a large-area $GaP(111)_B$ substrate could pave the way to new 2D/3D heterostructures with great interests in nanoelectronic and optoelectronic applications, especially in the development of new 2D-materials p-n junctions.

Acknowledgments

We acknowledge the financial support from the Tunne2D (ANR-21-CE24-0030) and ADICT (ANR-22-PEEL-0011) projects, as well as from the French technological network RENATECH and Region Hauts-de-France.

Data availability statement

Any data that support the findings of this study are included within the article.

References

[1] Novoselov K S, Jiang D, Schedin F, Booth T J, Khotkevich V V, Morozov S V and Geim A K 2005 Two-dimensional atomic crystals *Proc. Natl. Acad. Sci.* **102** 10451–3

[2] Wang Q H, Kalantar-Zadeh K, Kis A, Coleman J N and Strano M S 2012 Electronics and optoelectronics of two-dimensional transition metal dichalcogenides *Nat. Nanotechnol.* **7** 699–712

[3] Chhowalla M, Shin H S, Eda G, Li L-J, Loh K P and Zhang H 2013 The chemistry of two-dimensional layered transition metal dichalcogenide nanosheets *Nat. Chem.* **5** 263–75

[4] Bhimanapati G R, Lin Z, Meunier V, Jung Y, Cha J, Das S, Xiao D, Son Y, Strano M S, Cooper V R, Liang L, Louie S G, Ringe E, Zhou W, Kim S S, Naik R R, Sumpter B G, Terrones H, Xia F, Wang Y, Zhu J, Akinwande D, Alem N, Schuller J A, Schaak R E, Terrones M and Robinson J A 2015 Recent Advances in Two-Dimensional Materials beyond Graphene *ACS Nano* **9** 11509–39

[5] Mak K F, Lee C, Hone J, Shan J and Heinz T F 2010 Atomically Thin ${\mathrm{MoS}}_{2}$: A New Direct-Gap Semiconductor *Phys. Rev. Lett.* **105** 136805

[6] Splendiani A, Sun L, Zhang Y, Li T, Kim J, Chim C-Y, Galli G and Wang F 2010 Emerging Photoluminescence in Monolayer MoS2 *Nano Lett.* **10** 1271–5

[7] Kumar A and Ahluwalia P K 2012 Electronic structure of transition metal dichalcogenides monolayers 1H-MX2 (M = Mo, W; X = S, Se, Te) from ab-initio theory: new direct band gap semiconductors *Eur. Phys. J. B* **85** 186

[8] Jariwala D, Sangwan V K, Lauhon L J, Marks T J and Hersam M C 2014 Emerging Device Applications for Semiconducting Two-Dimensional Transition Metal Dichalcogenides *ACS Nano* **8** 1102–20

[9] Li M O, Esseni D, Nahas J J, Jena D and Xing H G 2015 Two-Dimensional Heterojunction Interlayer Tunneling Field Effect Transistors (Thin-TFETs) *IEEE J. Electron Devices Soc.* **3** 200–7

[10] Zhu Z Y, Cheng Y C and Schwingenschlögl U 2011 Giant spin-orbit-induced spin splitting in two-dimensional transition-metal dichalcogenide semiconductors *Phys. Rev. B* **84** 153402

[11] Riley J M, Mazzola F, Dendzik M, Michiardi M, Takayama T, Bawden L, Granerød C, Leandersson M, Balasubramanian T, Hoesch M, Kim T K, Takagi H, Meevasana W, Hofmann P, Bahramy M S, Wells J W and King P D C 2014 Direct observation of spin-polarized bulk bands in an inversion-symmetric semiconductor *Nat. Phys.* **10** 835–9

[12] Allain A and Kis A 2014 Electron and Hole Mobilities in Single-Layer WSe2 *ACS Nano* **8** 7180–5

[13] Fang H, Tosun M, Seol G, Chang T C, Takei K, Guo J and Javey A 2013 Degenerate n-Doping of Few-Layer Transition Metal Dichalcogenides by Potassium *Nano Lett.* **13** 1991–5

[14] Özden A, Ay F, Sevik C and Perkgöz N K 2017 CVD growth of monolayer MoS2: Role of growth zone configuration and precursors ratio *Jpn. J. Appl. Phys.* **56** 06GG05

[15] Huang J-K, Pu J, Hsu C-L, Chiu M-H, Juang Z-Y, Chang Y-H, Chang W-H, Iwasa Y, Takenobu T and Li L-J 2014 Large-Area Synthesis of Highly Crystalline WSe2 Monolayers and Device Applications *ACS Nano* **8** 923–30

[16] Liu B, Fathi M, Chen L, Abbas A, Ma Y and Zhou C 2015 Chemical Vapor Deposition Growth of Monolayer WSe2 with Tunable Device Characteristics and Growth Mechanism Study *ACS Nano* **9** 6119–27

[17] Clark G, Wu S, Rivera P, Finney J, Nguyen P, Cobden D H and Xu X 2014 Vapor-transport growth of high optical quality WSe2 monolayers a *APL Mater.* **2** 101101

[18] Liu H J, Jiao L, Xie L, Yang F, Chen J L, Ho W K, Gao C L, Jia J F, Cui X D and Xie M H 2015 Molecular-beam epitaxy of monolayer and bilayer WSe2: a scanning tunneling microscopy/spectroscopy study and deduction of exciton binding energy *2D Mater.* **2** 034004

[19] Park J H, Vishwanath S, Liu X, Zhou H, Eichfeld S M, Fullerton-Shirey S K, Robinson J A, Feenstra R M, Furdyna J, Jena D, Xing H G and Kummel A C 2016 Scanning Tunneling Microscopy and Spectroscopy of Air Exposure Effects on Molecular Beam Epitaxy Grown WSe2 Monolayers and Bilayers *ACS Nano* **10** 4258–67

[20] Yue R, Nie Y, Walsh L A, Addou R, Liang C, Lu N, Barton A T, Zhu H, Che Z, Barrera D, Cheng L, Cha P-R, Chabal Y J, Hsu J W P, Kim J, Kim M J, Colombo L, Wallace R M, Cho K and Hinkle C L 2017 Nucleation and growth of WSe2: enabling large grain transition metal dichalcogenides *2D Mater.* **4** 045019

[21] Zhang Y, Ugeda M M, Jin C, Shi S-F, Bradley A J, Martín-Recio A, Ryu H, Kim J, Tang S, Kim Y, Zhou B, Hwang C, Chen Y, Wang F, Crommie M F, Hussain Z, Shen Z-X and Mo S-K 2016 Electronic Structure, Surface Doping, and Optical Response in Epitaxial WSe2 Thin Films *Nano Lett.* **16** 2485–91

[22] Chen P, Pai W W, Chan Y-H, Sun W-L, Xu C-Z, Lin D-S, Chou M Y, Fedorov A-V and Chiang T-C 2018 Large quantum-spin-Hall gap in single-layer 1T' WSe2 *Nat. Commun.* **9** 2003

[23] Ugeda M M, Pulkin A, Tang S, Ryu H, Wu Q, Zhang Y, Wong D, Pedramrazi Z, Martín-Recio A, Chen Y, Wang F, Shen Z-X, Mo S-K, Yazyev O V and Crommie M F 2018 Observation of topologically protected states at crystalline phase boundaries in single-layer WSe2 *Nat. Commun.* **9** 3401

[24] He J, Hummer K and Franchini C 2014 Stacking effects on the electronic and optical properties of bilayer transition metal dichalcogenides MoS 2 , MoSe 2 , WS 2 , and WSe 2 *Phys. Rev. B* **89** 075409

[25] Zeng Z, Sun X, Zhang D, Zheng W, Fan X, He M, Xu T, Sun L, Wang X and Pan A 2019 Controlled Vapor Growth and Nonlinear Optical Applications of Large-Area 3R Phase WS2 and WSe2 Atomic Layers *Adv. Funct. Mater.* **29** 1806874

[26] Vergnaud C, Dau M-T, Grévin B, Licitra C, Marty A, Okuno H and Jamet M 2020 New approach for the molecular beam epitaxy growth of scalable WSe2 monolayers *Nanotechnology* **31** 255602

[27] Nie Y, Liang C, Zhang K, Zhao R, Eichfeld S M, Cha P-R, Colombo L, Robinson J A, Wallace R M and Cho K 2016 First principles kinetic Monte Carlo study on the growth patterns of WSe2 monolayer *2D Mater.* **3** 025029

[28] Nakano M, Wang Y, Kashiwabara Y, Matsuoka H and Iwasa Y 2017 Layer-by-Layer Epitaxial Growth of Scalable WSe2 on Sapphire by Molecular Beam Epitaxy *Nano Lett.* **17** 5595–9

[29] Mortelmans W, Kazzi S E, Mehta A N, Vanhaeren D, Conard T, Meersschaut J, Nuytten T, Gendt S D, Heyns M and Merckling C 2019 Peculiar alignment and strain of 2D WSe2 grown by van der Waals epitaxy on reconstructed sapphire surfaces *Nanotechnology* **30** 465601

[30] Aretouli K E, Tsoutsou D, Tsipas P, Marquez-Velasco J, Aminalragia Giamini S, Kelaidis N, Psycharis V and Dimoulas A 2016 Epitaxial 2D SnSe2/ 2D WSe2 van der Waals Heterostructures *ACS Appl. Mater. Interfaces* **8** 23222–9

[31] Pierucci D, Mahmoudi A, Silly M, Bisti F, Oehler F, Patriarche G, Bonell F, Marty A, Vergnaud C, Jamet M, Boukari H, Lhuillier E, Pala M and Ouerghi A 2022 Evidence for highly p-type doping and type II band alignment in large scale monolayer WSe2/Se-terminated GaAs heterojunction grown by molecular beam epitaxy *Nanoscale* **14** 5859–68

[32] Ohtake A and Sakuma Y 2021 Two-Dimensional WSe2/MoSe2 Heterostructures Grown by Molecular-Beam Epitaxy *J. Phys. Chem. C* **125** 11257–61

[33] Ueno K, Shimada T, Saiki K and Koma A 1990 Heteroepitaxial growth of layered transition metal dichalcogenides on sulfur-terminated GaAs{111} surfaces *Appl. Phys. Lett.* **56** 327–9

[34] Scimeca T, Watanabe Y, Berrigan R and Oshima M 1992 Surface chemical bonding of selenium-treated GaAs(111)A, (100), and (111)B *Phys. Rev. B* **46** 10201–6

[35] Nishikawa H, Saiki K and Koma A 1997 Surface morphology of S or Se terminated GaAs(111)B *Appl. Surf. Sci.* **113–114** 453–6

[36] Ohtake A, Goto S and Nakamura J 2018 Atomic structure and passivated nature of the Se-treated GaAs(111)B surface *Sci. Rep.* **8** 1220

[37] Ueno K, Abe H, Saiki K S K and Koma A K A 1991 Heteroepitaxy of Layered Semiconductor GaSe on a GaAs(111)B Surface *Jpn. J. Appl. Phys.* **30** L1352

[38] Rumaner L E, Olmstead M A and Ohuchi F S 1998 Interaction of GaSe with GaAs(111): Formation of heterostructures with large lattice mismatch *J. Vac. Sci. Technol. B Microelectron. Nanometer Struct. Process. Meas. Phenom.* **16** 977–88

[39] Vasil'ev V P and Gachon J-C 2006 Thermodynamic properties of III–V compounds *Inorg. Mater.* **42** 1176–87

[40] Baillargeon J N, Cheng K Y and Hsieh K C 1990 Surface structure of (100) GaP grown by gas source molecular beam epitaxy *Appl. Phys. Lett.* **56** 2201–3

[41] Foxon C T, Harvey J A and Joyce B A 1973 The evaporation of GaAs under equilibrium and non-equilibrium conditions using a modulated beam technique *J. Phys. Chem. Solids* **34** 1693–701

[42] TRAN MINH DUC 1998 Analyse de surface par ESCA. Analyse élémentaire et applications *Anal. Surf. Par ESCA Anal. Élémentaire Appl.* **P4** P2626.1-P2626.30

[43] Scofield J H 1976 Hartree-Slater subshell photoionization cross-sections at 1254 and 1487 eV *J. Electron Spectrosc. Relat. Phenom.* **8** 129–37

[44] Powell C J 2020 Practical guide for inelastic mean free paths, effective attenuation lengths, mean escape depths, and information depths in x-ray photoelectron spectroscopy *J. Vac. Sci. Technol. A* **38** 023209

[45] Jablonski A 2019 Evaluation of procedures for overlayer thickness determination from XPS intensities *Surf. Sci.* **688** 14–24

[46] Zemlyanov D Y, Jespersen M, Zakharov D N, Hu J, Paul R, Kumar A, Pacley S, Glavin N, Saenz D, Smith K C, Fisher T S and Voevodin A A 2018 Versatile technique for assessing thickness of 2D layered materials by XPS *Nanotechnology* **29** 115705

[47] Végh J 2006 The Shirley background revised *J. Electron Spectrosc. Relat. Phenom.* **151** 159–64

[48] Shirley D A 1972 High-Resolution X-Ray Photoemission Spectrum of the Valence Bands of Gold *Phys. Rev. B* **5** 4709–14

[49] Anon Office Locations | ULVAC-PHI, Inc.

[50] Mahmoudi A, Bouaziz M, Chapuis N, Kremer G, Chaste J, Romanin D, Pala M, Bertran F, Fèvre P L, Gerber I C, Patriarche G, Oehler F, Wallart X and Ouerghi A 2023 Quasi van der Waals Epitaxy of Rhombohedral-Stacked Bilayer WSe2 on GaP(111) Heterostructure *ACS Nano* **17** 21307–16

[51] M. McCreary K, Phillips M, Chuang H-J, Wickramaratne D, Rosenberger M, Stephen Hellberg C and T. Jonker B 2022 Stacking-dependent optical properties in bilayer WSe 2 *Nanoscale* **14** 147–56

[52] Litwin P M, Sales M G, Nilsson V, Balachandran P V, Constantin C and McDonnell S 2019 The effect of growth temperature and metal-to-chalcogen on the growth of WSe2 by molecular

beam epitaxy *Low-Dimensional Materials and Devices 2019* Low-Dimensional Materials and Devices 2019 vol 11085 (SPIE) pp 40–52

[53] Sales M G, Fields S, Jaszewski S, Smith S, Mimura T, Sarney W L, Najmaei S, Ihlefeld J F and McDonnell S 2021 WSe2 growth on hafnium zirconium oxide by molecular beam epitaxy: the effect of the WSe2 growth conditions on the ferroelectric properties of HZO *2D Mater.* **9** 015001

[54] Chastain J and King Jr R C 1992 *Handbook of X-Ray photoelectron spectroscopy* vol 40 (Perkin-Elmer Corporation)

[55] Xu M, Li L, Cai X, Liu Y, Chen Q, Guo J and Chu P K 2006 Nucleation and growth of amorphous carbon film on tungsten-implanted stainless steel substrates *Diam. Relat. Mater.* **15** 1580–4

[56] Dos Santos E P, Silva F L R, Gontijo R N, Alves J M, Ammar M-R and Fantini C 2020 Temperature dependence of the double-resonance Raman bands in bilayer WSe2 *Vib. Spectrosc.* **110** 103117

[57] De Luca M, Cartoixà X, Martín-Sánchez J, López-Suárez M, Trotta R, Rurali R and Zardo I 2020 New insights in the lattice dynamics of monolayers, bilayers, and trilayers of WSe2 and unambiguous determination of few-layer-flakes' thickness *2D Mater.* **7** 025004

[58] Williamson G K and Hall W H 1953 X-ray line broadening from filed aluminium and wolfram *Acta Metall.* **1** 22–31

[59] Ioffe Institute Basic Parameters of Gallium Phosphide (GaP)

[60] Waldrop J R, Grant R W and Kraut E A 1993 Measurement of AlP/GaP (001) heterojunction band offsets by x-ray photoemission spectroscopy *J. Vac. Sci. Technol. B Microelectron. Nanometer Struct. Process. Meas. Phenom.* **11** 1617–20

[61] Waldrop J R and Grant R W 1996 Measurement of AlN/GaN (0001) heterojunction band offsets by x-ray photoemission spectroscopy *Appl. Phys. Lett.* **68** 2879–81

[62] Rojas-Lopez R R, Brant J C, Ramos M S O, Castro T H L G, Guimarães M H D, Neves B R A and Guimarães P S S 2021 Photoluminescence and charge transfer in the prototypical 2D/3D semiconductor heterostructure MoS2/GaAs *Appl. Phys. Lett.* **119** 233101

[63] Yan X, Liu C, Li C, Bao W, Ding S, Zhang D W and Zhou P 2017 Tunable $SnSe_2/WSe_2$ Heterostructure Tunneling Field Effect Transistor *Small* **13** 1701478

[64] Wang X, Yan D, Zhu C, Feng Y, Guo T, Jia R, Qu K, Li L, Zhao T, Xiong Y, Farhan A, Lin Y, Wu L, Dong Y, Zhang S, Chen X and Song X 2023 Ultrasensitive photodetector based on 2D WS_2/AgInGaS quantum dots heterojunction with interfacial charge transfer *2D Mater.* **10** 045020